

Article

# Wireless Power Transfer for Battery Powering System

Tianfeng Wang <sup>1</sup>, Xin Liu <sup>1</sup> , Nan Jin <sup>2</sup>, Houjun Tang <sup>1</sup>, Xijun Yang <sup>1,\*</sup> and Muhammad Ali <sup>1</sup> 

<sup>1</sup> School of Electronic Information and Electrical Engineering, Shanghai Jiao Tong University, Shanghai 200240, China; wangtf1992@sjtu.edu.cn (T.W.); Liu\_xin@sjtu.edu.cn (X.L.); hjtang@sjtu.edu.cn (H.T.); engrmak.ee@sjtu.edu.cn (M.A.)

<sup>2</sup> College of Electric and Information Engineering, Zhengzhou University of Light Industry, Zhengzhou 450002, China; jinnan@zzuli.edu.cn

\* Correspondence: yangxijun@sjtu.edu.cn; Tel.: +86-021-34204604

Received: 18 August 2018; Accepted: 5 September 2018; Published: 7 September 2018



**Abstract:** The LCL topology (formed by an LC tank with a transmitting coil) is extensively utilized in wireless power transfer (WPT) systems with the features of a constant resonant current and ability to disconnect load abruptly. However, it requires high input voltage, which limits its utilization in battery powering scenarios (12~24 V). A current-fed inverter (CFI) is applied to the LCL-S (a compensation capacitor in series with the receiving coil) WPT systems to boost the input voltage, thereby getting a higher resonant current in the transmitting side (Tx). To facilitate the voltage regulation in the receiving side (Rx), a semi-active bridge (SAB) is introduced into the system, which further boosts the output voltage by a lower frequency switching at different duty ratios. Rigorous mathematical analysis of the proposed system is carried out and design guidelines are subsequently derived. Moreover, a power loss reduction is realized by zero voltage switch (ZVS) of the four switches in the Tx which are deduced and presented. Simulations and experiments are added to verify the proposed system. Consequently, a 93.3% system efficiency (DC-to-DC efficiency) is obtained using the proposed topology. Optimization techniques for a higher efficiency are included in this study.

**Keywords:** current-fed inverter; LCL-S topology; semi-active bridge; soft switching; voltage boost; wireless power transfer

## 1. Introduction

Nowadays, wireless power transfer (WPT) technology is a leading research field due to the wide spread electronic devices that can benefit from this technology. For instance, electric vehicles can get rid of electrical hazards caused by wire snapping and reduce on-board battery burden by dynamic charging [1–3]. Medical implants benefit from the increased power supply without the penalty of a greater bulk [4,5]. In addition, a WPT charger can power multiple loads simultaneously without lots of wires and complex connections. Accordingly, it can be predicted that WPT will be a good assistant of, or an alternative to the plug-in power transfer in various voltage rate systems. The advantages and prospects have already ignited a hot interest all over the world, and related studies are burgeoning.

In WPT systems, the compensation topologies are very crucial for high efficiency and power rates by reducing and even cancelling leakage inductance. Research on compensation topologies and their features are continually carried out and new ideas have been investigated and put forward as well [6–9]. Many research works rely on four basic topologies, namely series-series (SS), series-parallel (SP), parallel-parallel (PP), and parallel-series (PS) [10]. However, to meet special or practical requirements, such as constant current/voltage output [7,11] and the endurance of load tripping, hybrid compensation approaches like LC and LCC [12,13] have been put forward. Although, the hybrid topologies introduce more passive components into the system and may add power loss and system bulk, their benefits outweigh the shortcoming for demand and security reasons. Among

these topologies, the LCL topology, formed by an LC tank with a transmitting coil, is regarded as an ideal network used in the transmitting side (Tx), due to its ability to maintain the transmitting current constant and independent of the reflected impedance of the receivers [11,14]. Thus, the induced voltage in every receiving side (Rx) is steady. Moreover, if the disconnection happens in the four basic topologies, urgent protection would be needed, or the circuit is over-current burned. The LCL topology can endure unexpected load disconnection, so it is rather promising in practice. Accordingly, the LCL topology is applied in the Tx in this literature due to these features.

Nevertheless, this topology requires a large input voltage or small receiving coil inductance to augment the transmitting current and induce a high voltage in the Rx. Decreasing the coil inductance will lead to a small mutual inductance and a voltage decreasing in the Rx. Hence, enlarging the input voltage is recommended. The input voltage is 400 V in Ref. [9], and the input voltage of the Evatran products is 220 V. Otherwise, the output voltage can be small, only 5 V in Ref. [11] due to the small input of 26 V. For some power sources, such as photovoltaic panels and batteries, the voltage rating of each cell is very low. The output voltage of a solar cell module is around 12~24 V, and the nominal voltage of a lead-acid battery with six cells is only 12 V. Simply increasing the number of panels and cells in series can surge the system bulk, pressure and insulation requirement, thereby being impractical for solar system applications, wearable devices, and other portable equipment. In addition, the WPT technology may be adopted as an aid for safety and reliability in some internal sub-systems, where only low-voltage sources can be provided.

To extend the WPT technology and LCL topology to battery powering system and wirelessly power the loads within the 12~24 V input range, front-end boost circuits are in great need. Inserting the traditional boost circuits before the inverter is a good solution and also generally used. High efficiency of the boost circuits can be obtained due to the maturity of boost techniques. However, lots of components (an active switch, a power diode, a comparably large inductor, and a capacitor) and auxiliary circuits (control circuits and drivers) are needed. In contrast, the Z-source/quasi-Z-source networks boost the output voltage by shorting the end-rear bridge, which can be realized by the full bridge inverter itself and the extra control circuits are not required [15]. Nevertheless, two inductors and two capacitors are added so the losses caused by these components increase inevitably and the system may incur maloperations caused by the resonant networks [16–18]. On the other hand, large inductances are required in the Z-source network to suppress the ripples and prevent the discontinuous current mode [19]. Hence these two mentioned circuits will increase the bulk of the power system, which may cause difficulty in carrying or assembling.

To realize a high conversion gain and a compact size with a simpler topology, a current-fed inverter (CFI) is a good alternative in WPT systems. The CFI only contains a full bridge inverter and two identical front-end inductors so that the power conversion stages are reduced with an improvement in reliability [20,21]. Compared with the voltage source inverter (VSI) in series with a boost circuit, the CFI has a simpler circuit and easier control method. The control and response rates are also improved due to the compact stages. Compared with the Z-source inverter (ZSI), the CFI has less components and reduces the total harmonic distortion (THD) of the input current. Moreover, the switches in the CFI can operate ZVS from inductive impedance to capacitive impedance and the top-side switches can be turned OFF softly in some scenarios.

Conventionally, there are two kinds of schemes to regulate the output voltage. One scheme is to apply a diode rectifier in the Rx but conduct the optimal charge control in the Tx (the source voltage level shift, the duty ratio adjustment, etc.). This scheme predigests the Rx complexity but needs frequent and quick communications. Another scheme is to control the Rx by itself, which lowers the communication demand. Two circuits have already been proposed: inserting the buck-boost converter connected in series with the rectifier [22] or replacing the rectifier with an active bridge [23]. The former involves a large inductor and more control circuits. The latter requires a complicated controller and complex auxiliary circuits with increasing receiving volume, which is not as compact as mobile devices require. Considering the trade-off between the size and communication complexity,

an active switch replaces one diode of the rectifier and regulates the load voltage in this literature. This semi-active bridge (SAB) can regulate the output by being operated at a variable frequency and duty ratio. Specially, the SAB can boost the output, which can obtain higher voltage than the diode rectifier. Different from the switches in an active bridge that must operate at a high and precise resonant frequency, the switch in SAB can conduct at a lower frequency. Additionally, the complex control protocols and negotiation required by the active bridge [24] are not necessary for the SAB.

The paper is structured as follows: Section 2 depicts the proposed circuit diagram of the WPT system, followed by its operating principle. The capability of soft switching is also elaborated upon. Section 3 models the proposed system with mathematical analyses of the system parameters. Guidelines are provided on the configurations of the inductors, coils, and loads. In Section 4, simulations are implemented, and results are presented and compared. To further support and verify the theoretical analysis and simulation accuracy, a prototype is developed and experimental results are provided in Section 5. A 93.3% system efficiency (DC-to-DC efficiency) is achieved, and the output voltage is within twice to four times that of the input. Optimization techniques for higher efficiency are included. Finally, Section 6 concludes the paper.

## 2. Proposed Topology

### 2.1. System Composition

A block diagram of the proposed topology with one receiver is demonstrated in Figure 1. In the Tx, the CFI contains a clamp capacitor  $C_o$ , two identical front-end inductors ( $L_1$  and  $L_2$ ), and four switches ( $Q_1, Q_{1a}, Q_2$ , and  $Q_{2a}$ ), which can be regarded as an assembly of two boost converters [20,21]. A combination of the switching pattern and the inductors implement the boost function, and the amplitude of the output voltage is equal to the capacitor voltage  $V_C$  across  $C_o$ . For the resonant network, the LCL topology and series compensation topology is employed in the Tx and Rx, respectively. As for the Rx, the SAB supersedes the rectifier, where a bottom side diode is replaced by a controllable switch  $Q_s$ .

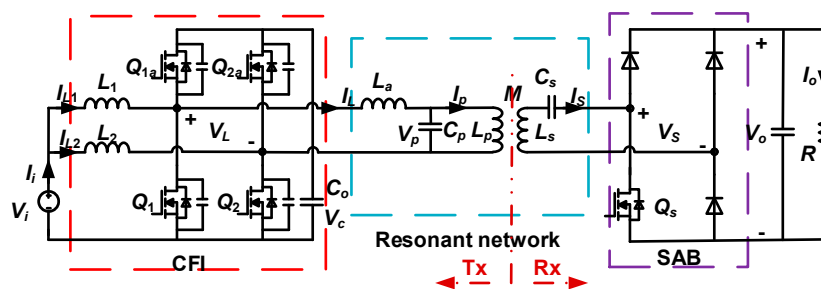


Figure 1. Proposed circuit diagram of WPT systems with one receiver.

In this paper, bold italic letters symbolize the phasors and the italic letters symbolize the real numbers or RMS values. In Figure 1,  $L_p$  and  $C_p$  represent the Tx coil inductance and its compensation capacitance.  $L_s$  and  $C_s$  represent the Rx coil inductance and its compensation capacitance.  $L_a$  and  $M$  represent the compensation inductance and mutual inductance.  $V_i$  and  $I_i$  are the input voltage and input current from the source.  $V_L$  and  $I_L$  are the output voltage and current of the CFI.  $V_p$  and  $I_p$  are the voltage across and the current through Tx coil.  $V_s$  and  $I_s$  are the input voltage of the SAB and the resonant current in the resonant tank.

### 2.2. Operation Patterns in Tx

Theoretically, four states exist in the full bridge. However, if the top-side switches are both ON, the charging circuits for  $L_1$  and  $L_2$  are broken and the voltage-boost function cannot be accomplished. Thus, three states are conducted in the CFI. Defining the duty ratio of  $Q_1$  and  $Q_2$  as  $d_s$ ,  $d_s$  should be

above 0.5 to prevent  $Q_{1a}$  and  $Q_{2a}$  being both ON. The unequal PWM control [25] is adopted in this paper and the corresponding waveforms are depicted in Figure 2a. The four switches all conduct at a resonant frequency  $f_s$ . When  $Q_{1a}$  and  $Q_2$  are ON,  $V_L$  is positive,  $L_1$  is discharged but  $L_2$  is charged, as shown in Figure 2b. When  $Q_{2a}$  and  $Q_1$  are ON,  $V_L$  is negative,  $L_1$  is charged but  $L_2$  is discharged, as shown in Figure 2d. When the bottom-side switches are ON,  $V_L$  is zero, both  $L_1$  and  $L_2$  are charged, as shown in Figure 2c,e.

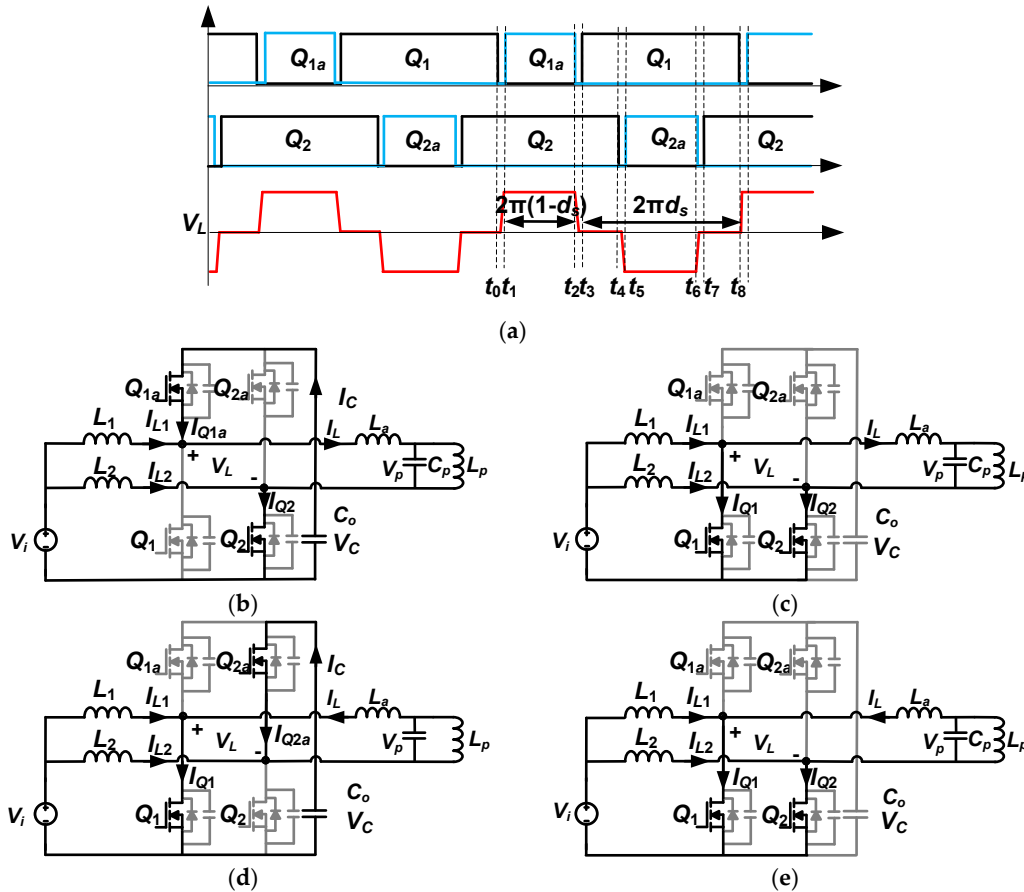


Figure 2. (a) Typical operation patterns of the CFI, (b)  $t_1 \sim t_2$ ; (c)  $t_3 \sim t_4$ ; (d)  $t_5 \sim t_6$ ; (e)  $t_7 \sim t_8$ .

The current stress of each switches is estimated as

$$\begin{cases} I_{Q1a\max} = I_{Lm} - I_{L1\min} \\ I_{Q1\max} = I_{Lm} + I_{L1\max} \\ I_{Q2a\max} = I_{Lm} - I_{L2\min} \\ I_{Q2\max} = I_{Lm} + I_{L2\max} \end{cases} \quad (1)$$

As can be seen, the bottom-side switches suffer higher stresses than the top-side switches. According to the boost converter properties [26], the peak-to-peak current ripple and the maximum value of the inductor currents in Discontinuous Conduction Mode (DCM) are larger than those in Continuous Conduction Mode (CCM) under the same load conditions. Due to the rear-end resonant current,  $L_1$  and  $L_2$  will not enter DCM but quasi-CCM, where the currents through the inductors reverse their direction and the inductors are charged by the resonant network. The current ripple in quasi-CCM is large and the switches will suffer large stresses, according to Equation (1). Consequently, the CFI in this paper is recommended to operate in CCM to decrease the current stresses of the bottom switches. Thus, the two front-end inductors  $L_1$  and  $L_2$  should be well designed.

### 2.3. Operation Patterns in Rx

In the receiving side,  $Q_s$  operates at frequency  $f_{Q_s}$ . The ratio of  $f_s$  and  $f_{Q_s}$  is denoted as  $n (>1)$ , and the duty ratio of  $Q_s$  is denoted as  $d_{Q_s}$ . Parts of the waveforms and the corresponding patterns are illustrated in Figure 3. The direction of the dark arrow of  $I_s$  is chosen as a reference direction and the red dotted lines denote the actual current paths. When  $Q_s$  is turned OFF, it functions as a common diode. The duty ratio of  $Q_s$  is 0.5 and the corresponding waveforms of  $V_s$ ,  $I_s$ ,  $I_p$  are presented in Figure 3a.  $I_s$  flows as shown in Figure 3b,c, where  $V_s$  is positive and negative, respectively. When  $Q_s$  is turned ON, the anode of  $D_1$  is directly connected with the anode of  $D_3$  as shown in Figure 3d,e. When  $I_s$  is positive, as shown in Figure 3d, it flows straight from one end of the compensation capacitor to the end of the Tx coil, that is, the load  $R$  is cut off from the resonant source and  $V_s$  drops to zero. When  $I_s$  is negative, as shown in Figure 3e, however, it flows through  $D_2$  and powers the parallel capacitor and the load. At that time,  $V_s$  is negative as shown in Figure 3a. Therefore,  $I_s$  resonates at  $f_s$ , while the frequency of its envelope line is  $f_{Q_s}$ . On the other hand, the amplitude of  $I_p$  can be deemed as a constant value, although the equivalent load changes frequently as mentioned. Hence, the Rx can achieve a stable induced voltage ignoring the rapid change of the equivalent impedance, which is also the reason for choosing the LCL topology as the SAB and LCL complement each other.

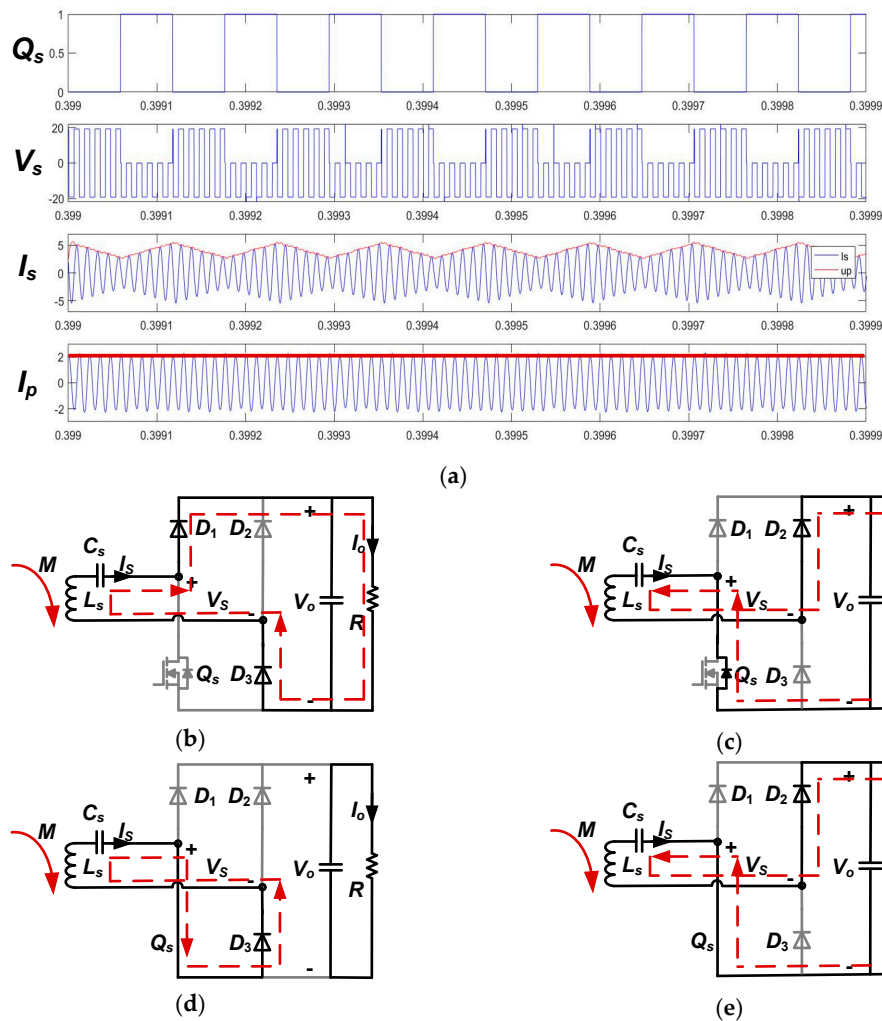


**Figure 3.** Typical waveforms and operation patterns of the SAB (a) waveforms of the SAB (b) current path when  $Q_s$  is OFF and  $I_s$  is positive (c) current path when  $Q_s$  is OFF and  $I_s$  is negative (d) current path when  $Q_s$  is ON and  $I_s$  is positive (e) current path when  $Q_s$  is ON and  $I_s$  is negative.

2.4. Soft-Switching Capability

In the Tx, the soft-switching operation is accomplished by the CFI and the clamp capacitor  $C_o$ .  $Q_1$  and  $Q_{1a}$  are chosen to illustrate the soft-switching process. The analysis of  $Q_2$  and  $Q_{2a}$  is fundamentally the same as the analysis of  $Q_1$  and  $Q_{1a}$  due to the topology symmetry. The current paths are depicted in Figure 4.

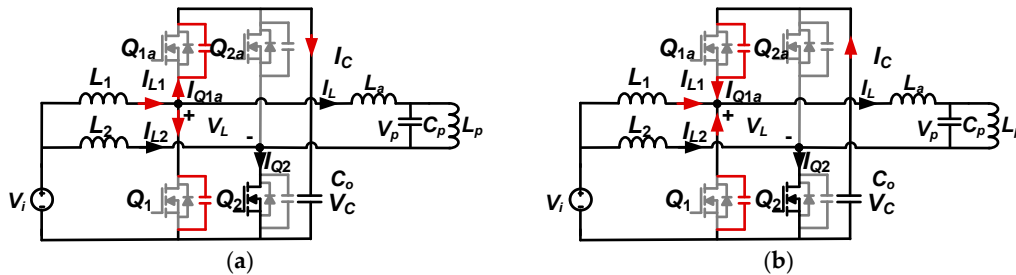


Figure 4. Current paths for CFI conducting ZVS (a) state before  $Q_{1a}$  is on  $t_0 \sim t_1$ ; (b) state before  $Q_1$  is on  $t_2 \sim t_3$ .

Figure 4a shows the state before  $Q_{1a}$  is ON, where  $I_{L1}$  reaches its maximum value. The difference between  $I_{L1}$  and  $I_L$  is positive. The current difference charges the parallel capacitor of  $Q_{1a}$ ,  $C_{Q1a}$ , and discharges the parallel capacitor of  $Q_1$ ,  $C_{Q1}$ . Figure 4b shows the state before  $Q_1$  is ON, where  $I_{L1}$  reaches its minimum value. At that time, the difference between  $I_{L1}$  and  $I_L$  is negative. Then,  $C_o$  also provides current to charge  $C_{Q1}$  and discharge  $C_{Q1a}$ . Hence, ZVS of  $Q_{1a}$  and  $Q_1$  are achieved.

To turn OFF the top-side switches softly [27],  $I_{L1}$  should be a bit larger than  $I_L$  before  $Q_{1a}$  is OFF so that  $I_{Q1a}$  will reverse direction from Figure 5a to Figure 5b. Then, when  $Q_{1a}$  is turned OFF, the freewheeling current can flow through the parallel diode, providing a condition for the soft-switching OFF [27].

In comparison with the VSI, the inductors in the CFI can provide the current directly for soft switching, thereof getting rid of the rear-end resonant current limitation. Accordingly, the soft switching can be more likely accomplished.

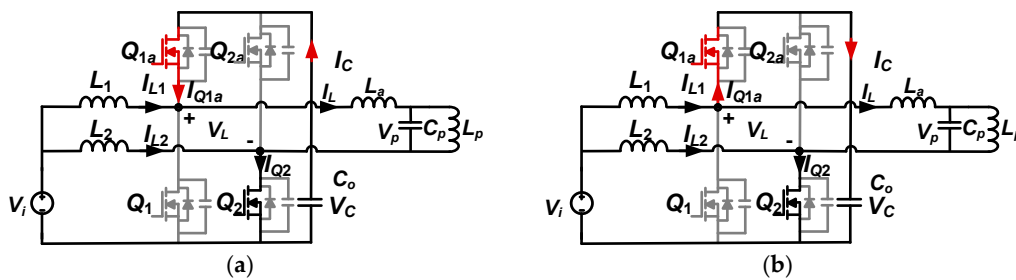


Figure 5. Current paths before turning OFF  $Q_{1a}$  (a) preclude to the hard OFF; (b) preclude to the soft OFF.

To guarantee the inductors working in CCM and the minimum value of  $I_{L1}$  larger than  $I_L$ , the inductance should be large, accompanied with the increase of the internal resistance and power loss caused by the inductors. Thus, the inductance should be set at a reasonable value.

In the Rx, the soft-switching operation [27] can also be realized by  $Q_s$  being turned ON/OFF when the current and the voltage are negative. If  $Q_s$  is turned OFF when  $I_s$  is positive and  $V_s$  is zero, the current path will suddenly change from Figure 3d to Figure 3b, leading to a surge of  $V_s$  and the hard-switching OFF  $Q_s$ . Additionally, if  $Q_s$  is turned ON when  $I_s$  and  $V_s$  are positive, the current path will suddenly change from Figure 3b to Figure 3d, leading to a plunge of  $V_s$  and the hard-switching ON of  $Q_s$ . The distortion waveform of  $V_s$  is demonstrated in Figure 6b. However, if  $Q_s$  is turned

ON/OFF when  $I_s$  is negative, the current pattern switches between Figure 3c and Figure 3e. As can be seen, the voltage output in Figure 6c is ideal and the soft-switching operation is also achieved. To prevent this distortion,  $Q_s$  should be turned ON when  $I_s$  is negative, which can be achieved alone in the Rx. In contrast, the dual active bridge (DAB) strictly demands the synchronization [28], otherwise, the system becomes unstable and power oscillations occur.

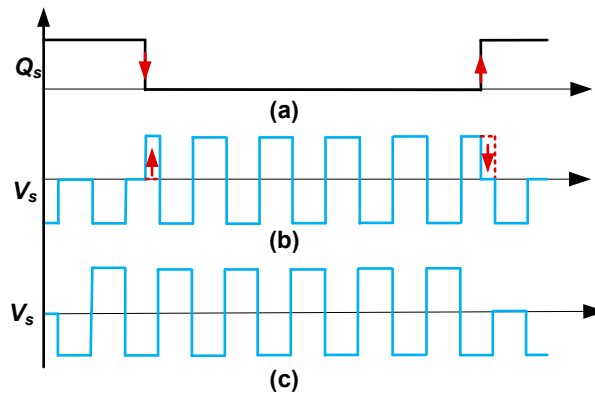


Figure 6. Difference of  $V_s$  caused by the switch time (a)  $Q_s$  switch time; (b) distortion of  $V_s$ ; (c) ideal waveform of  $V_s$ .

### 3. Mathematical Modeling and Configuration

#### 3.1. Equivalent Circuit Model

To model and analyze the proposed system, an equivalent circuit is established as shown in Figure 7.  $Z_p$ ,  $Z_{sref}$ , and  $R_{ac}$  denote the Tx equivalent impedance, the reflected impedance from the Rx and the equivalent ac resistance calculated in a receiving switching period, respectively.  $Z_{pt}$ ,  $Z_{sref}$ , and  $R_{act}$  denote the three impedances calculated in a resonant period.  $r_p$  and  $r_s$  denote the inner resistances of the Tx coil and the Rx coil. Besides,  $L_a$  is designed to be identical to  $L_p$ . Considering the power losses, inner resistance of  $L_a$  is represented by  $r_{La}$ . In addition,  $r_L$  denotes the inner resistance of  $L_1$  and  $L_2$ . The Tx switching frequency and the resonant frequency are both equalized to  $f_s$ .

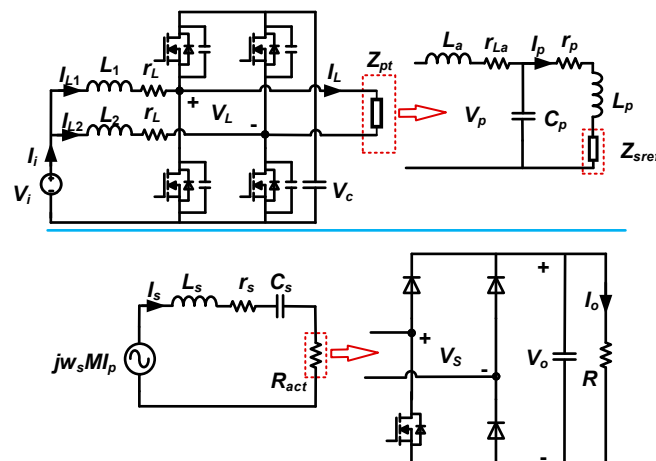


Figure 7. Equivalent circuit diagram.

Thus,  $Z_{pt}$  is resistive and deduced as:

$$Z_{pt} = j\omega_s L_a + r_{La} + \frac{(j\omega_s L_p + Z_{sref} + r_p) \frac{1}{j\omega_s C_p}}{j\omega_s L_p + Z_{sref} + r_p + \frac{1}{j\omega_s C_p}} = \frac{(\omega_s L_p)^2}{Z_{sref} + r_p} + r_{La} \approx \frac{(\omega_s L_p)^2}{Z_{sref} + r_p}, \quad (2)$$

where,  $Z_{srefl}$  is equal to

$$Z_{srefl} = \frac{(\omega_s M)^2}{R_{act} + r_s}. \tag{3}$$

Based on the boost model, the amplitude of the square wave  $V_L$  is derived as:

$$V_{Lm} = V_C = \frac{V_i}{1 - d_s}. \tag{4}$$

Thus, the RMS value of the fundamental harmonic of  $V_L$  is deduced as:

$$V_{L1} = 2\sqrt{2}V_i \frac{\sin \pi d_s}{\pi(1 - d_s)}. \tag{5}$$

Then, the output current of CFI in a resonant period is:

$$I_L = \frac{V_{L1}}{Z_{pt}} = \frac{2\sqrt{2}V \sin \pi d_s}{\pi(1 - d_s)(\omega_s L_p)^2} \left[ \frac{(\omega_s M)^2}{R_{act} + r_s} + r_p \right]. \tag{6}$$

Obviously,  $I_L$  is load-dependent and its RMS value  $I_L$  will decrease with the augment of  $R_{act}$ . However, the RMS value of branch current  $I_p$  is calculated as:

$$I_p = \frac{V_{L1} \cdot (Z_{srefl} + r_p)}{(\omega_s L_p)^2} \frac{\frac{1}{j\omega_s C_p}}{\frac{1}{j\omega_s C_p} + j\omega_s L_p + Z_{srefl} + r_p} = \frac{V_{L1}}{j\omega_s L_p}, \tag{7}$$

which signifies that  $I_p$  is independent of the Rx characteristics but proportional to the input voltage. Accordingly, high input voltage  $V_L$  is recommended to maintain a large resonant current. According to the mutual inductance theory, the induced voltage  $V_s$  in the Rx keeps steady if  $I_p$  is constant.

In the Rx, the model can be presented as:

$$j\omega_s M I_p = \left[ j\omega_s L_s + r_s + \frac{1}{j\omega_s C_s} + R_{act} \right] I_s = [r_s + R_{act}] I_s, \tag{8}$$

which implies that the induced voltage and the receiving current are in-phase.

### 3.2. Equivalent Resistance of SAB

To analyze the impact of duty ratio  $d_{Qs}$  and receiving switching frequency  $f_{Qs}$  ( $=f_s/n$ ) on  $R_{ac}$ ,  $R_{act}$ , and output voltage  $V_o$ , the harmonic approximation method and extended describing function are utilized. Assuming that the induced voltage  $v(t)$ , receiving current  $i_{sL}(t)$ , and compensation capacitor voltage  $v_{sC}(t)$  can be approximated by fundamental terms and the former two are in same phase due to the resistive impedance, it has

$$\begin{cases} v(t) = \omega_s M I_{pm} \sin \omega_s t \\ i_{sL}(t) = i_{sLs}(t) \sin \omega_s t \\ v_{sC}(t) = v_{sCc}(t) \cos \omega_s t \end{cases}, \tag{9}$$

where, the envelope terms are slowly time varying at  $f_s/n$ .

By utilizing the extended describing method,  $V_s$  whose waveform is depicted in Figure 3a, can be approximated as

$$v_s(t) \approx f_s(n, d_{Qs}, V_o) \sin \omega_s t. \tag{10}$$

The extended describing function  $f_s(n, d_{Q_s}, V_o)$  can be calculated by Fourier expansions and given as

$$f_s(n, d_{Q_s}, V_o) = -\frac{d_{Q_s}}{2} V_o + \sum_{k=1}^{\infty} \left[ a_k \cos k \frac{\omega_s}{n} t + b_k \sin k \frac{\omega_s}{n} t \right], \quad (11)$$

where the coefficients are

$$\begin{cases} a_k = \frac{V_o}{\pi k} \left[ \sum_{i=1}^{2n-2d_{Q_s}n} (-1)^i \sin k\varphi \left| \frac{\pi i}{\pi(i-1)/n} \right. - \sum_{i=n-d_{Q_s}n}^{n-1} \sin k\varphi \left| \frac{\pi(2i+1)/n}{2\pi i/n} \right. \right] \\ b_k = \frac{V_o}{\pi k} \left[ \sum_{i=1}^{2n-2d_{Q_s}n} (-1)^{i-1} \cos k\varphi \left| \frac{\pi i}{\pi(i-1)/n} \right. + \sum_{i=n-d_{Q_s}n}^{n-1} \cos k\varphi \left| \frac{\pi(2i+1)/n}{2\pi i/n} \right. \right] \end{cases} \quad (12)$$

However, it is difficult to get an analytical solution on the relationship between  $f_s, d_{Q_s}, V_o,$  and  $R_{ac}$ , since the switching frequency is below the resonant frequency and the equivalent impedance in each resonant period is different from others, which is totally contrary to the small-signal model condition [29]. Nevertheless, a trend estimation can be conducted by analyzing the extreme cases. Since the SAB disconnects the load OFF and ON, it can be assumed that when the load is OFF, the equivalent impedance  $R_{ac}$  decreases. To validate this assumption and estimate the relation between  $d_{Q_s}$  and  $R_{ac}$ , two extreme cases ( $d_{Q_s} = 0$  and  $d_{Q_s} = 1$ ) are considered. The corresponding waveforms are presented in Figure 8.

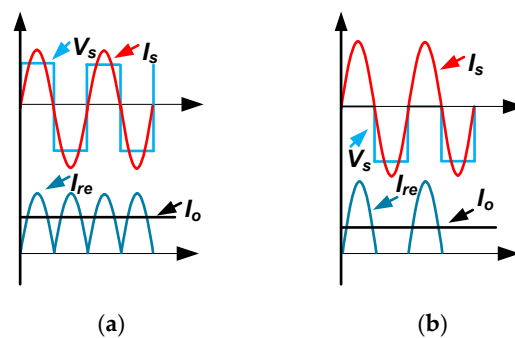


Figure 8. Typical waveforms of the Rx under different duty ratios (a)  $d_{Q_s} = 0$ ; (b)  $d_{Q_s} = 1$ .

When  $Q_s$  stays OFF, that is  $d_{Q_s} = 0$ , the SAB works as a diode rectifier. The typical waveforms are depicted in Figure 8a, where  $I_{re}$  represents the output current of the SAB. Thus, the equivalent ac resistance reaches the maximum as given in [30]:

$$\begin{cases} R_{act} = R_{ac} \\ R_{acmax} = \frac{8R}{\pi^2} \end{cases} \quad (13)$$

However, when  $Q_s$  stays ON, that is  $d_{Q_s} = 1$ , the anode of  $D_1$  is directly connected with the anode of  $D_3$ , waveforms change to Figure 8b and the ac load accordingly, is

$$\begin{cases} R_{act} = R_{ac} \\ R_{acmax} = \frac{2\sqrt{2}R}{\pi^2} \end{cases} \quad (14)$$

It can be found that  $R_{ac}$  decreases when  $d_{Q_s}$  increases. Besides, on basis of Equation (6), it can be drawn that the input current  $I_L$  and input power will rise as  $d_{Q_s}$  increases, and the dc output  $V_o$  boost as well due to the energy principles. Thus, the voltage boost function is accomplished.

Assuming that the power loss caused by SAB can be ignored, the power fetched from the Tx is equal to the load power, that is,

$$\frac{V_o^2}{R} = I_p^2 \frac{(\omega_s M)^2}{R_{act} + r_s} \frac{R_{act}}{R_{act} + r_s}. \quad (15)$$

Hence, by substituting Equations (5), (7), (13) and (14) into Equation (15), the range of the output voltage is estimated as:

$$\frac{2\sqrt{2}\pi MR}{L_p(8R + \pi^2 r_s)} \frac{\sin \pi d_s}{(1 - d_s)} V_i \leq V_o \leq \frac{2^{0.75}\pi MR}{L_p(2\sqrt{2}R + \pi^2 r_s)} \frac{\sin \pi d_s}{(1 - d_s)} V_i, \quad (16)$$

which shows the dc load can acquire a wide range of output. Besides, the output voltage  $V_o$  can be higher than the input voltage  $V_i$  with proper configurations.

### 3.3. Soft-Switching Design in Tx

The power fetched from the CFI  $P_L$  during a resonant period is deduced, with Equations (5) and (6), as:

$$P_L = \frac{8V_i^2}{(\omega_s L_p)^2} \frac{\sin^2 \pi d_s}{\pi^2(1-d_s)^2} \left[ \frac{(\omega_s M)^2}{R_{act} + r_s} + r_p \right] \geq \frac{8V_i^2}{(\omega_s L_p)^2} \frac{\sin^2 \pi d_s}{\pi^2(1-d_s)^2} \left[ \frac{(\omega_s M)^2}{R_{acmax} + r_s} + r_p \right] = P_{Lmin}. \quad (17)$$

Assuming that the magnitude of power loss caused by the switches,  $L_1$ ,  $L_2$ , and  $C_o$  can be ignored as compared to that of  $P_L$ ,  $P_L$  is therefore equal to the DC input power  $P_i$ , which can be presented as:

$$P_i = \frac{1}{2} V_i \left[ 2I_{imin} + \frac{V_i}{L} (2d_s - 1) T_s \right], \quad (18)$$

where,  $L = L_1 = L_2$ ,  $I_{imin}$  is the minimum value of the DC input current, illustrated in Figure 9, and can be calculated as

$$I_{imin} = 2I_{L1min} + \frac{V_i T_s}{2L}. \quad (19)$$

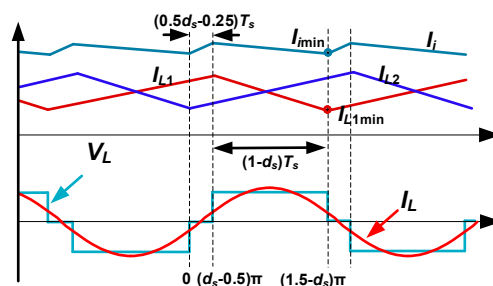


Figure 9. Typical waveforms of the CFI.

Accordingly,  $I_{L1min}$  can be calculated with Equations (17)–(19) as:

$$I_{L1min} = \frac{4V_i \sin^2 \pi d_s}{\pi^2(1 - d_s)^2 Z_{pt}} - \frac{V_i T_s}{2L} d_s. \quad (20)$$

To prevent the system from quasi-CCM,  $I_{L1min}$  should be above zero. To make  $I_{L1min} > 0$ ,  $L$  can be deduced from Equation (20) with Equation (2) as:

$$L > \frac{T_s d_s}{8} \frac{(\omega_s L_p)^2}{\frac{\sin^2 \pi d_s}{\pi^2(1-d_s)^2} \frac{(\omega_s M)^2}{R_{act} + r_s} + r_p}. \quad (21)$$

On the other hand, to complete the soft-switching OFF  $Q_{1a}$ , it demands

$$I_{L1min} > I_L|_{\varphi=1.5\pi-\pi d_s} \tag{22}$$

Defining  $Q$  as the loaded quality factor of the Tx,  $Q$  can be calculated as:

$$Q = \frac{Z_{srefl}}{\omega_s L_p} = \frac{\omega_s k^2 L_s}{(R_{act} + r_s)} \tag{23}$$

where  $k$  denotes the coupling coefficient.

When  $Q$  is large, the output current of CFI is sinusoidal as presented in Figure 9. To complete soft-switching OFF  $Q_{1a}$ , Equation (22) is written as:

$$I_{L1min} > \sqrt{2} I_L \sin\left(\frac{3}{2}\pi - \pi d_s\right), \tag{24}$$

that is,  $L$  is deduced from Equation (24) as:

$$L > \frac{T_s d_s}{8 \frac{\sin \pi d_s}{\pi(1-d_s)} \left[ \frac{\sin \pi d_s}{\pi(1-d_s)} + \cos \pi d_s \right]} \frac{(\omega_s L_p)^2}{\frac{(\omega_s M)^2}{R_{act} + r_s} + r_p} \tag{25}$$

Since  $d_s$  is above 0.5, the right of Equation (21) is larger than that of Equation (25) and reaches its maximum when  $d_s$  is 0.5. Hence, the inductance should meet the requirement as:

$$L > \frac{\pi^2}{64 f_s} \frac{(\omega_s L_p)^2}{\frac{(\omega_s M)^2}{R_{act} + r_s} + r_p} \tag{26}$$

Nevertheless, considering the inner resistances and power losses of the two inductors at high input current,  $L$  cannot increase blindly otherwise the system efficiency will degrade.

However, when  $Q$  is small (i.e.,  $Q < 1$  according to the MATLAB and PLECS simulation),  $I_L$  distorts and  $I_{Q1a}$  can never reverse direction no matter how large  $L$  is, thereby failing soft-switching OFF  $Q_{1a}$  and  $Q_{2a}$ . In practice, the inner resistances of the coils will surge significantly with the increase of the coil inductance. On the other hand, the LCL topology requires rigorous manufacturing technique to reduce the coil resistance since the losses of the coil resistors in LCL topology far outweigh that in series compensation topology. Accordingly,  $L_p$  and  $M$  are usually small, which inevitably results in a small  $Q$  and distortion of  $I_L$ . Simply increasing  $L_s$  can reduce the receiving efficiency due to the enlarged coil resistance, leading to the system efficiency decreasing as well. Thus, there is a trade-off between the soft-switching OFF and system efficiency.

### 3.4. Optimal Load

To evaluate the system efficiency variation caused by the change of the equivalent impedance, the optimal load is calculated. Given that the power loss caused by the CFI is hard to theoretically calculated, the transmitting efficiency  $\eta$ , defined as the ratio of the CFI output power to the equivalent ac power, is presented to calculate the optimal load for the CFI and approximate the system efficiency.  $\eta$  can be written with Equations (3), (5)–(7) as:

$$\eta = \frac{I_p^2 Z_{srefl}}{V_{L1} I_L} = (\omega_s M)^2 \frac{R_{act}}{r_p R_{act}^2 + (\omega_s M)^2 R_{act} + 2r_s r_p R_{act} + (\omega_s M)^2 r_s + r_s^2 r_p} \tag{27}$$

The derivative of Equation (27) is calculated as:

$$\frac{d\eta}{dt} = (\omega_s M)^2 \frac{-r_p R_{act}^2 + (\omega_s M)^2 r_s + r_s^2 r_p}{\left[ r_p R_{act}^2 + (\omega_s M)^2 R_{act} + 2r_s r_p R_{act} + (\omega_s M)^2 r_s + r_s^2 r_p \right]^2}. \quad (28)$$

To obtain the highest  $\eta$ , Equation (28) should be equal to zero, that is,

$$R_{act} = \sqrt{\frac{(\omega_s M)^2 r_s}{r_p} + r_s^2}. \quad (29)$$

To maintain a large output voltage,  $L_s$  is deliberately designed much larger than  $L_p$ , whereas,  $r_s$  is 75 times  $r_p$  in this paper. Hence, Equation (29) can be simplified as:

$$R_{act} = \omega_s M \sqrt{r_s / r_p}. \quad (30)$$

By substituting Equation (30) into Equation (23), Equation (23) is rewritten as:

$$Q = k \sqrt{\frac{L_s r_p}{r_s L_p}}. \quad (31)$$

If  $R_{act}$  is set as the optimal value, and Equation (31) is above 1, the soft-switching OFF  $Q_{1a}$  and  $Q_{2a}$  can be achieved.

#### 4. Simulation and Verification

To validate the analysis and the aforementioned assumptions, simulations are implemented. According to Equation (7), the Tx coil inductance  $L_p$  is set as a small value, 15.5  $\mu\text{H}$ , to obtain a large current and small resistance 8 m $\Omega$  as well. The coil-to-coil gap is fixed at 10 cm and the coupling coefficient  $k$  is 0.2. Since the receiving coil adopt the series compensation topology, the coil inductance is designed to a large value and set as a large value as 274.7  $\mu\text{H}$  but followed by a large resistance, 0.3  $\Omega$ . To obtain high efficiency based on Equations (27) and (29), the dc load is set as 52  $\Omega$  according to Equation (13). It is worth noting that efficiency will drop when  $Q_s$  turns ON, because  $R_{act}$  will gradually deviate from the optimum. The forward voltage drop of the diode  $V_F$  is 0.6 V and the on resistance of the MOSFET is 80 m $\Omega$ . The configurations are listed in Table 1.

Table 1. Model Parameters.

Parameter	Value	Parameter	Value
Load R	52 $\Omega$	Input voltage $E_V$	24 V
Transmitting switching frequency $f_s$	85 kHz	Mutual inductance $M$	18 $\mu\text{H}$
Transmitting inductance $L_p$	15.5 $\mu\text{H}$	Transmitting inner resistance $r_p$	8 m $\Omega$
Receiving inductance $L_s$	274.7 $\mu\text{H}$	Receiving inner resistance $r_s$	0.3 $\Omega$
Compensation inductance $L_a$	15.5 $\mu\text{H}$	Compensation inner resistance $r_{La}$	0.04 $\Omega$
DC inductance $L_1$ & $L_2$	51 $\mu\text{H}$	DC inner resistance $r_L$	0.2 $\Omega$
Transmitting capacitance $C_p$	222 nF	Receiving capacitance $C_s$	12.8 nF
Clamp capacitance $C_o$	470 $\mu\text{F}$	Transmitting duty ratio $d_s$	0.7
Forward voltage drop of diode $V_F$	0.6 V	On resistance of MOSFET $R_{on}$	80 m $\Omega$

##### 4.1. Soft-Switching Realization

When  $Q_s$  operates at different duty ratios, the equivalent ac impedance varies. Thus, the variation range of the loaded quality factor is [0.14, 0.40] calculated by Equation (23). The range of the minimum of the front-end inductance  $L$  is calculated as [38.6  $\mu\text{H}$ , 107.4  $\mu\text{H}$ ] by Equation (21). When the SAB works as a common diode rectifier, the minimum of  $L$  surges to 107.4  $\mu\text{H}$ , which also means a bulky

size and large inner resistance. Although the large inductors prevent circulating current, the saved power can hardly compensate the losses caused by the inner resistance, and hence  $L$  is configured a medium value as  $51 \mu\text{H}$  with  $0.2 \Omega$ . Then, after  $Q_s$  operates, the circulating current will be eliminated. Simulations are fulfilled at different  $d_{Q_s}$ . The simulation waveforms of  $Q_{1a}$  and  $I_{L1}$  are depicted in Figure 10. Figure 10a illustrates the waveforms where  $R$  is  $52 \Omega$  and  $Q_s$  stays OFF. The whole system efficiency is 94.5%. Figure 10b illustrates the waveforms where  $R$  is  $52 \Omega$  and  $Q_s$  operates as 8500 Hz with  $d_{Q_s} = 0.5$ . The efficiency is 94.1%. Figure 10c demonstrates the waveforms where  $R$  is  $52 \Omega$  and  $Q_s$  stays ON. The efficiency is 90.8%. Figure 10d demonstrates the waveforms where  $R$  is  $20 \Omega$  and  $Q_s$  stays ON.

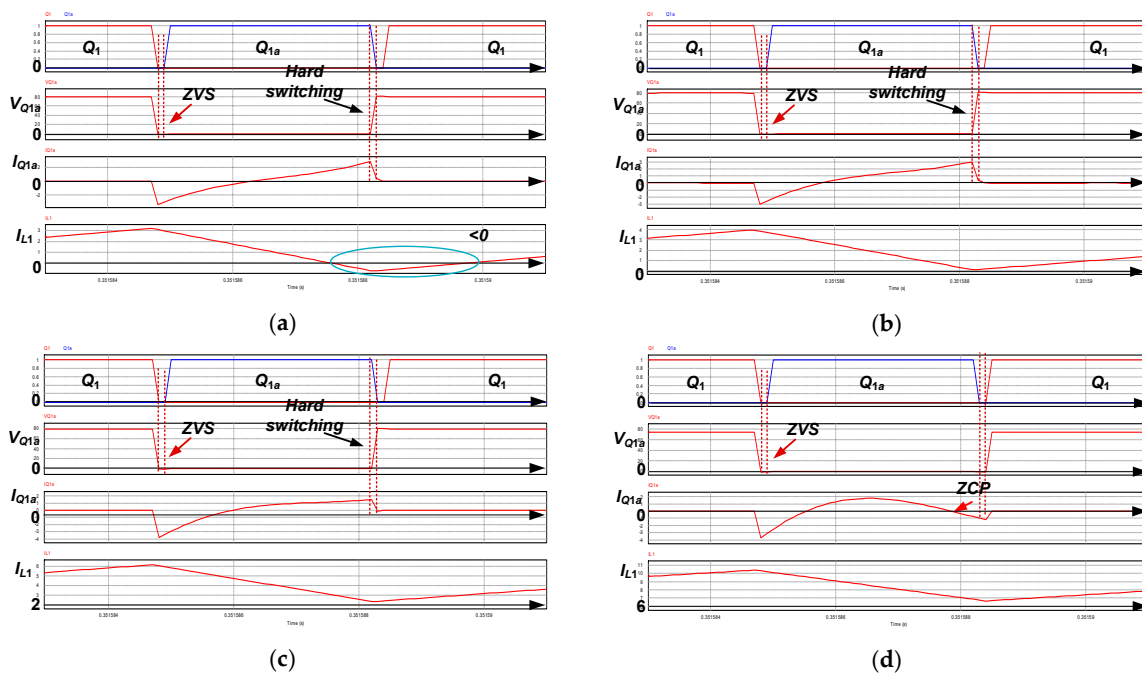


**Figure 10.** Typical waveforms of  $Q_{1a}$  and  $I_{L1}$  with a same  $L$  but different  $d_{Q_s}$ : (a)  $R = 52 \Omega$ ,  $d_{Q_s} = 0$ ,  $\eta = 94.5\%$ ; (b)  $R = 52 \Omega$ ,  $d_{Q_s} = 0.5$ ,  $\eta = 94.1\%$ ; (c)  $R = 52 \Omega$ ,  $d_{Q_s} = 1$ ,  $\eta = 90.8\%$ ; (d)  $R = 20 \Omega$ ,  $d_{Q_s} = 1$ .

As Figure 10 shows, before  $Q_{1a}$  is ON, the voltage across  $Q_{1a}$ ,  $V_{Q_{1a}}$ , has already reached zero. Hence, ZVS is accomplished in above mentioned four cases. However, when  $R$  is  $52 \Omega$  and  $Q$  is below 1,  $Q_{1a}$  is hard-switching OFF. Additionally, when  $R_{ac}$  is small, the theoretical minimum of  $L$  is above  $51 \mu\text{H}$  so that the quasi-CCM occurs, and  $I_{L1}$  is below zero for a period of time, which means  $L_1$  is charged by the resonant network and a circulation current exists in  $L_1$  and  $L_2$ . When  $R_{ac}$  augments, the value  $51 \mu\text{H}$  satisfies Equation (21) and the circulating current is eliminated as illustrated in Figure 10b,c. Two conclusions can be drawn. Firstly, the deviation of the optimal load will reduce the efficiency comparing Figure 10b with Figure 10c. Secondly, the elimination of the circulation current can increase the efficiency as can be observed by comparing Figure 10b with Figure 10a,c. Besides, when the load decreases and  $Q$  increases above 1, a zero-cross point (ZCP) occurs before  $Q_{1a}$  is OFF and  $I_{Q_{1a}}$  reverses its direction as Figure 5b demonstrates. Then  $I_{Q_{1a}}$  can flow through the parallel diode for freewheeling rather than be forced to abruptly discontinue, which achieves the soft-switching OFF  $Q_{1a}$  as analyzed.

#### 4.2. Equivalent Resistance of SAB and Variation Trend

In Section 3, the equivalent resistance of SAB  $R_{act}$  is regarded as a pure resistance according to the analysis on full-wave rectifier [30] and half-wave rectifier. To validate this assumption, we have  $Q_s$  working at 8500 Hz with  $d_{Q_s} = 0.5$ . Waveforms of  $I_p$ ,  $I_s$ , and  $V_s$  are presented in Figure 11. The purple dotted lines show that  $I_p$  lags  $90^\circ$  behind  $I_s$  so  $j\omega_s M I_p$  is in phase with  $I_s$  which conforms to Equation

(8). Moreover, the dark dotted lines show that the fundamental voltage  $V_s$  and  $I_s$  are also in phase. These phases verify a purely resistive equivalent impedance.

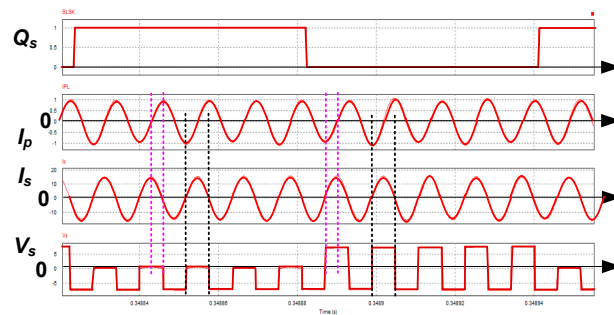


Figure 11. Phase differences in the Tx.

To further evaluate the impact of frequency ratio  $n$  and duty ratio  $d_{Qs}$  on the system, the simulation results of the output dc voltage, transferred power, and efficiency under different conditions are depicted and compared in Figure 12.  $Q_s$  works at three frequencies, 8500 Hz (i.e.,  $n = 10$ ), 17,000 Hz (i.e.,  $n = 5$ ), and 42,500 Hz (i.e.,  $n = 2$ ).

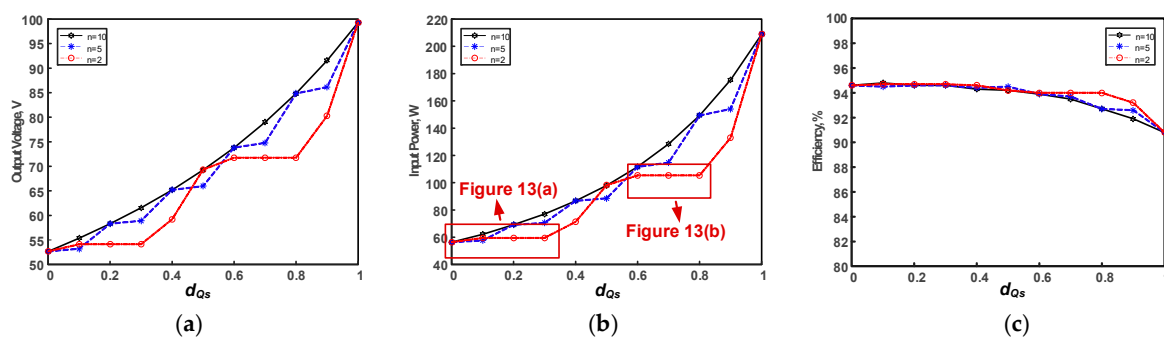
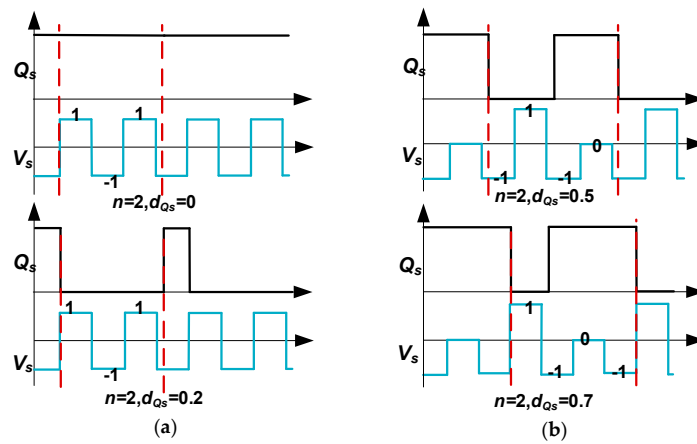


Figure 12. System performance under different frequencies and duty ratios (a) output voltage (b) input power (c) efficiency.

From Figure 12a, it is observable that the output voltage grows with the increase of  $d_{Qs}$ , which verifies the voltage boost function as claimed and also reflects the rise of  $R_{ac}$  according to Equation (15). Besides, the increase of input power can prove the negative correlation between  $R_{act}$  and  $I_L$  as already presented in Equation (6). In addition, it can be observed that the system has the same input power and output voltage once the product of  $n$  and  $d_{Qs}$  is integral and  $d_{Qs}$  stays the same. The integer of  $n \cdot d_{Qs}$  means that a switching-ON period of  $Q_s$  contains an integral multiple of the resonant period, as does the switching-OFF period. On the other hand, an identical  $d_{Qs}$  means an identical proportion of the on-load time and idle time as presented in Figure 6. Accordingly, the equivalent ac load remains the same. If the switching-ON period of  $Q_s$  does not contain an integral multiple of the resonant period, the output voltage and input power may rise disproportionately as the blue line and the red line show. This phenomenon occurs because the effective proportions of the on-load time and idle time does not change. The examples in Figure 13 should suffice to demonstrate the stated where  $n \cdot d_{Qs} \leq 0.5$  or  $0.5 \leq n \cdot (1 - d_{Qs}) \leq 1$ .



**Figure 13.** Impact of  $n$  and  $d_{Q_s}$  on the equivalent impedance when  $n \cdot d_{Q_s}$  is small (a)  $n \cdot d_{Q_s} \leq 0.5$  (b)  $0.5 \leq n \cdot (1 - d_{Q_s}) \leq 1$ .

Therefore, a large frequency ratio, i.e., a low operation of the receiving side, allows the power to grow in a linear fashion. However, if  $Q_s$  works at a low frequency, the ripple of the output voltage gets large, which may be unbearable for battery charging. For instance, the system output voltages, input powers, and efficiencies are totally identical when  $Q_s$  operates at 8500 Hz and 4250 Hz, theoretically. Nevertheless, the ripples at 4250 Hz operation are three times those at 8500 Hz. Thus, there is a trade-off between the system variation linearity and the output ripples considering the practical application. It is worth noting that the switching loss of the MOSFETs is not considered in the simulation, which will rise with the increase of the operating frequency. In this paper,  $Q_s$  conducts at 8500 Hz as recommended.

**5. Experimental Result and Discussions**

To validate and evaluate the aforementioned analyses and simulations, a practical prototype was established and tested. Figure 14 shows the laboratory prototype and its component configurations have been already tabulated in Table 1 in Section 4. However, the actual value of the load was 51.2  $\Omega$  and the switching frequencies of the Tx and the Rx were 86 kHz and 8600 Hz, respectively. The DSP TMS320F28335 (San Jose, CA, USA) was used as the digital controller in this system. MPP (Ni-Fe-Mo) cores were chosen for  $L_1, L_2$ , and  $L_a$  for lower loss. The coil diameter is 37 cm and the coil-to-coil gap is set as 10 cm. The inductances are measured by a Keysight E4980AL (Santa Rosa, CA, USA) LCR meter under 86 kHz.

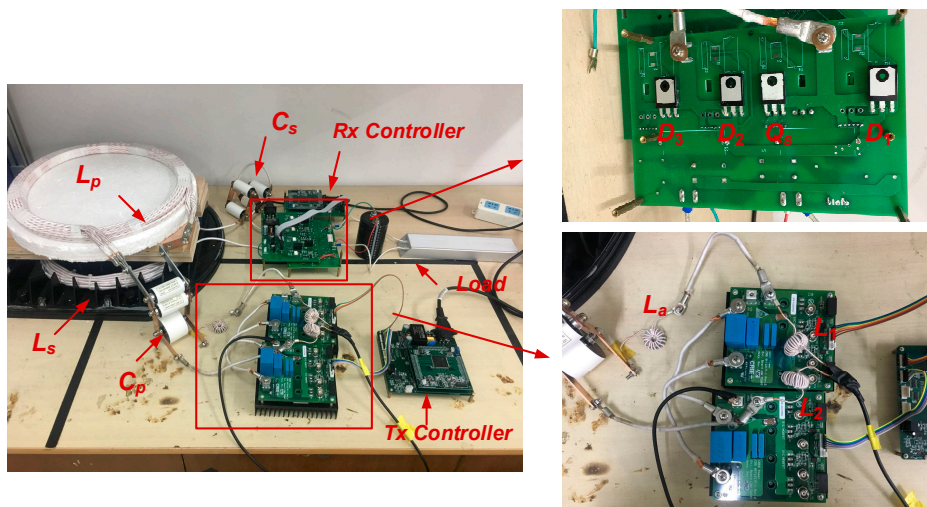


**Figure 14.** Prototype of the proposed system.

### 5.1. Soft-Switching Realization

All the four switches on the transmitter can perform ZVS under wide power variation as analyzed. The dead time is set as 2% of the resonant period. The waveforms of the four switches in three cases ( $Q_s$  stays OFF,  $d_{Q_s} = 0.5$ , and  $Q_s$  stays ON) are presented in Figure 15. The input power is the smallest when  $Q_s$  keeps OFF, and the output current  $I_L$  distorts as claimed in Section 3 and is presented in Figure 15b. Nevertheless, ZVS of the four switches are achieved successfully as presented in Figure 15a. After  $Q_s$  operates, both the input power and the loaded quality factor rise. When  $d_{Q_s} = 0.5$ ,  $I_L$  is different from each other in every resonant period but  $I_{L1}$  keeps periodic variation. Hence, the current  $I_{L1}-I_L$  provided for ZVS keeps changing in Figure 15d. However, ZVS of the top-side switches is still realized and ZVS of the bottom-side is also achieved most of the time as illustrated in Figure 15c. When  $Q_s$  stays on,  $I_L$  approximates to sine. As can be seen, all the switches can conduct ZVS as presented in Figure 15e. However, the soft switching-OFF for the top side switches is not achieved. The red lines in Figure 15b,d,f denote the result of  $I_{L1}$  minus  $I_L$ , and the waveforms, when  $Q_{1a}$  is going to be turned OFF, are emphasized by the ellipse. At that time, the result  $\Delta I$  being negative denotes that there is a current flowing from the source electrode of  $Q_{1a}$  to its drain electrode. Therefore, the hard-switching OFF is inevitable.

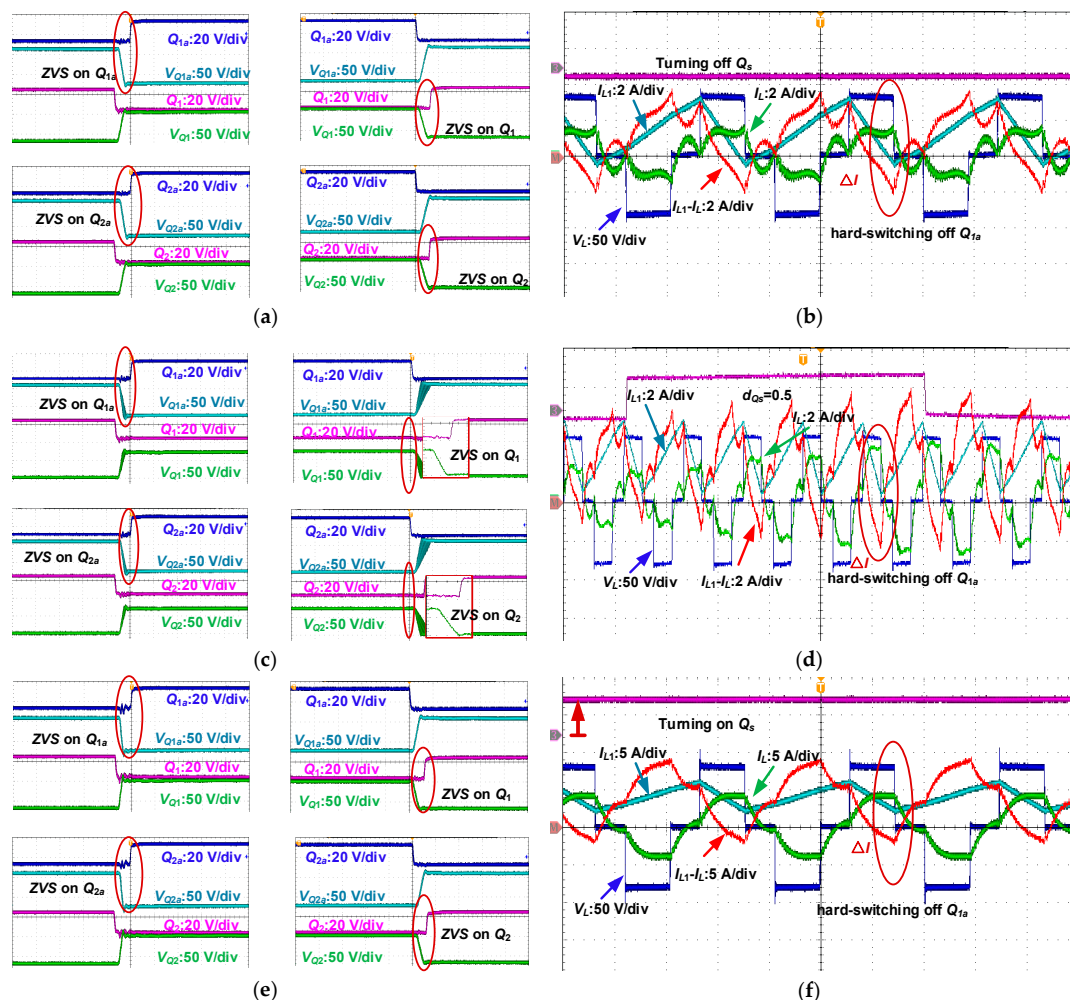


**Figure 15.** ZVS waveforms under different cases: (a) ZVS of four switches when  $d_{Q_s} = 0$ ; (b) current waveforms when  $d_{Q_s} = 0$ ; (c) ZVS of four switches when  $d_{Q_s} = 0.5$ ; (d) current waveforms when  $d_{Q_s} = 0.5$  (e) ZVS of four switches when  $d_{Q_s} = 1$ ; (f) current waveforms when  $d_{Q_s} = 1$ .

On the Rx, soft switching of  $Q_s$  can also be achieved. Figure 16a,b demonstrate the waveforms of  $V_s$  and  $V_{Q_s}$  at different  $d_{Q_s}$  conditions. It can be observed that if  $Q_s$  is turned ON/OFF when  $V_s$  is negative and  $V_{Q_s}$  is zero as illustrated in Figure 3c,e, voltage distortion does not occur. Nevertheless, in practice,  $n \cdot d_{Q_s}$  is not always an integer, thereby resulting in three switching situations:  $Q_s$  hard switching ON,  $Q_s$  hard switching OFF, and  $Q_s$  hard switching ON/OFF. To estimate the hard-switching impact,  $d_{Q_s}$  is set as 0.4, and  $n$  is set as 10. Then  $Q_s$  works in soft-switching ON/OFF case as shown in Figure 16c and hard-switching ON/OFF as shown in Figure 16d. When  $V_s$  and  $V_{Q_s}$  are positive,  $Q_s$  is turned ON. The current path switches from Figure 3b to Figure 3d compulsively, leading to a distortion denoted by the ellipse 1 in Figure 16d. When  $V_s$  and  $V_{Q_s}$  are positive,  $Q_s$  is turned OFF. The current path switches from Figure 3d to Figure 3b compulsively, leading to a distortion denoted by the ellipse 2 in Figure 16d. It is found that when the input power is 103.2 W, the former efficiency is 93.3%, a little higher than the latter efficiency of 92.7%, saving switching loss of 0.5 W.

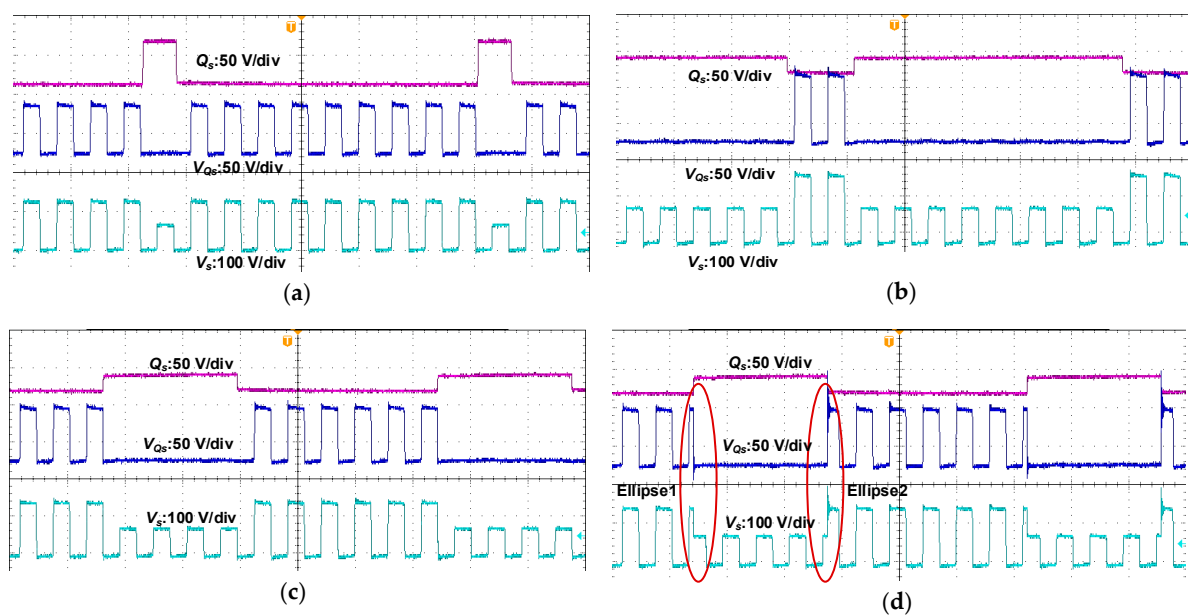


**Figure 16.** Waveforms of  $V_s$  and  $V_{Q_s}$  with different  $d_{Q_s}$ : (a)  $d_{Q_s} = 0.1$  (b)  $d_{Q_s} = 0.8$  (c)  $d_{Q_s} = 0.4$  (d)  $d_{Q_s} = 0.4$  but hard switching.

Additionally,  $I_{L1}$  is observed to analyze the impact of the equivalent load and the front-end inductance. At first, the value of  $L_1$  and  $L_2$  is set as  $51 \mu\text{H}$ . When  $Q_s$  stays OFF, both the input power and the equivalent impedance are small. The inductance,  $51 \mu\text{H}$ , is much less than the proposed value,  $107 \mu\text{H}$ . Part of  $I_{L1}$  is below zero as depicted in Figure 17a, thereby showing a circulating current exists in  $L_1$  and  $L_2$ . However, with the increase of the equivalent impedance, the value of  $51 \mu\text{H}$  meets the requirements. Hence, the circulating current is eliminated and  $I_{L1}$  is always above zero as presented in Figure 17b,c.

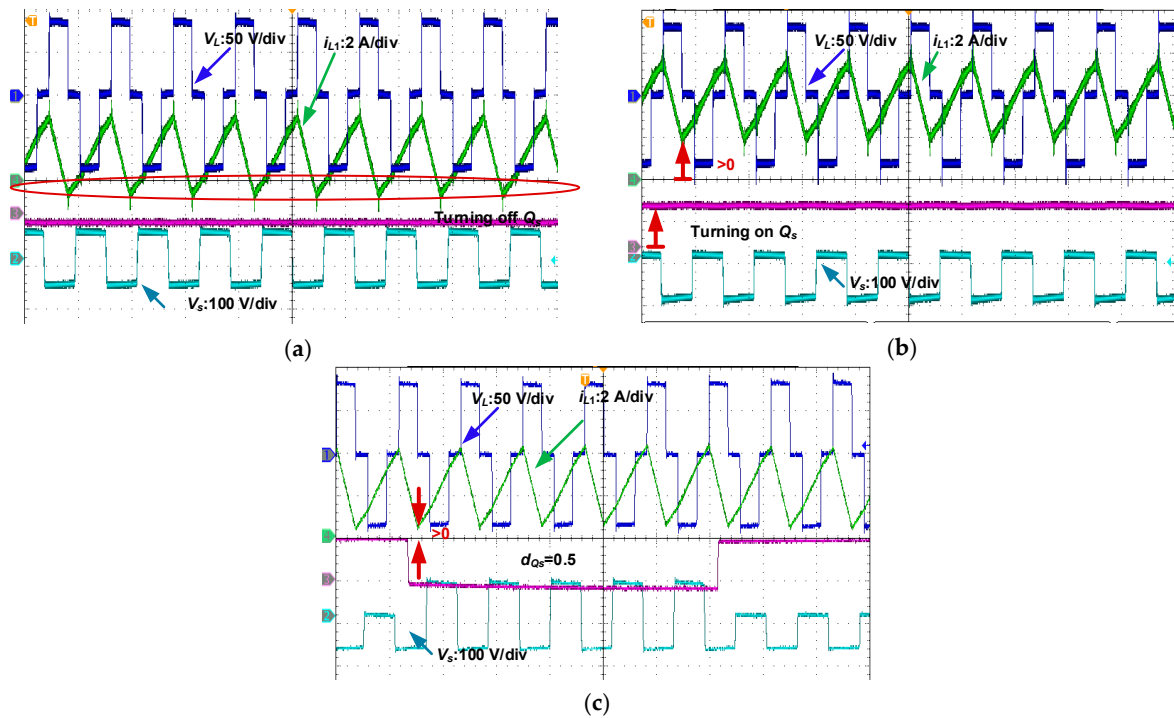


**Figure 17.** Waveforms of  $I_{L1}$ ,  $V_p$ , and  $V_s$ :  $L_1$  is 51  $\mu$ H but the equivalent impedance  $R_{act}$  changes (a)  $Q_s$  stays OFF,  $R_{act}$  reaches the maximum, part of  $I_{L1}$  is below zero; (b)  $Q_s$  stays ON,  $R_{act}$  reaches the minimum,  $I_{L1}$  is above zero; (c)  $Q_s$  operates with  $d_{Qs} = 0.5$ ,  $I_{L1}$  is above zero.

### 5.2. Efficiency and Loss Estimation

Figure 18 demonstrates the system efficiency and the loss estimation. The blue dashed line presents the simulation result and the dark line presents the experimental result. Figure 18a shows that a higher output voltage more than the input voltage 24 V, is accomplished and boosted further after  $Q_s$  working. The results support the calculation of Equation (16). The experimental output voltage at the beginning is the same as the simulation but deviates from the theoretical value with the increasing of  $d_{Qs}$  and system operation power. Besides, the input power of the experiment is a little higher than that of the simulation power when  $d_{Qs}$  is below 0.5, whereas this situation reverses after  $d_{Qs}$  becomes above 0.5. This difference is mainly caused by the modelling of the SAB in the simulations. At first, the practical forward voltage drop is not invariably 0.6 V but increase from 0.6 V to 0.8 V. The deterioration of the voltage drop can be regarded as the increase of  $R_{act}$ , thereby decreasing the practical input power according to Equation (17). In addition, the input current surging from 2.8 A to 8.7 A and the temperature rise may result in the parameter drift and the difference presented in Figure 18. High efficiency is achieved over the variation of  $d_{Qs}$  as depicted in Figure 18c. Although the efficiency drops with  $d_{Qs}$  rising, 88% efficiency is sustained. In general, the results of the established simulation and experimental prototype are accordant and validate the proposed topology and methods. High efficiency can still be obtained though three inductors are added into the WPT system.

Based on the data presented in Figure 18a,b, the power losses can be calculated. When  $Q_s$  stays OFF, the power loss is 5.31 W, where the losses caused by the rectifier (0.6 V drop) and the inner resistance of the front-end inductors  $L_1$  and  $L_2$  (0.2  $\Omega$ ) are obvious and make the main percentage as presented in Figure 18d, where  $d_{Qs}$  is 0. After  $Q_s$  operates and the power transfer rate rises, the loss ratio of the front-end inductors and the Rx coil increases as shown in Figure 18d where  $d_{Qs}$  is 1. Hence, there are two ways to improve the system efficiency. One is decreasing the high-frequency resistance by optimizing the inductors and determining a proper value according to Equations (21) and (25). Another method is reducing the receiver coil resistance with optimal coil manufacturing. Otherwise the output rate reduces according to Equations (16) and (17).

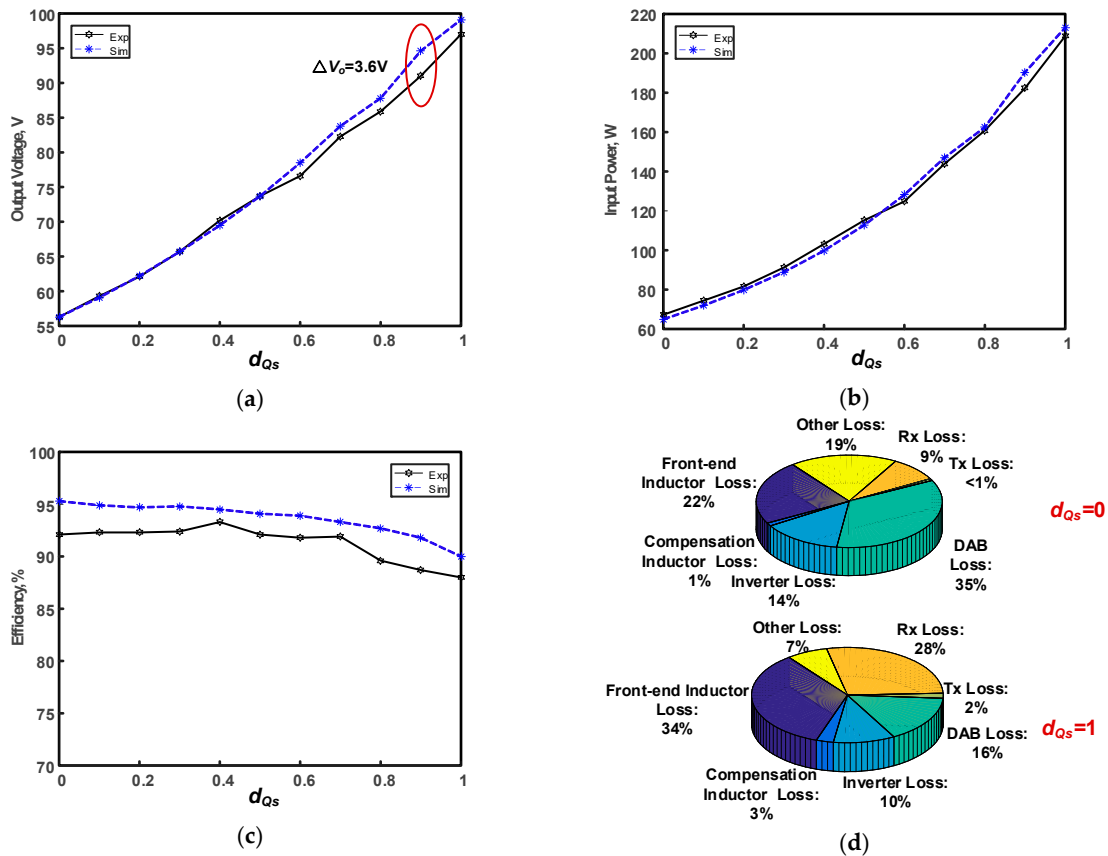


Figure 18. Efficiency and power loss comparison (a)  $V_o$  vs.  $d_{Qs}$ ; (b)  $P_i$  vs.  $d_{Qs}$ ; (c)  $\eta$  vs.  $d_{Qs}$ ; (d) loss analysis of extreme working cases.

### 5.3. Load Tripping

To further present the advantage of LCL topology to the load tripping as aforementioned, experiments are added for validation. For convenience, the Tx coil will be artificially removed to imitate the load tripping scenario. Figure 19 shows the variation of  $I_L$  and  $I_p$ . Over the working time,  $I_p$  stays constant even though the load is off, which is in accordance with the analysis of Equation (7). However,  $I_L$  varies when the load is off and on.  $I_L$  becomes small when the load is off, but becomes large again when the load is reconnected. Moreover, it can be seen that the whole system remains safe all the time.

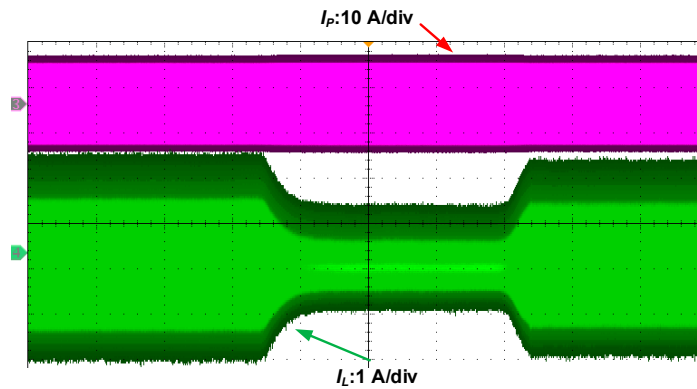


Figure 19. Waveforms of  $I_L$  and  $I_p$  when load tripping occurs.

## 6. Conclusions

The LCL topology is regarded as an ideal network used in the WPT systems due to its constant resonant current in the Tx coil and independence of the reflected impedance of the receivers. However, this topology requires a large source voltage to generate transmitting current and induced voltage of receivers, which limits its application in the low voltage scenarios, such as 12~24 V. This paper applied a CFI into WPT systems to boost the voltage for LCL. ZVS of the switches were accomplished under wide range of power rates and also under serious current distortion. The ability of the CFI to turn OFF the top-side switches softly was also deduced and presented in this paper.

On the receiving side, a SAB was proposed and applied to regulate and boost the output voltage and the system power. The SAB allows a lower frequency and reduces the communication requirement compared with the DAB synchronization. Higher output voltage and wide variation range were accomplished.

Guidelines on the parameter design of the front-end inductance, coils and optimal load were elaborately presented. Although more inductors were added into the system, a peak efficiency of 93.3% was obtained and the lowest efficiency was maintained at 88% with proper configuration. Both simulations and experimental results are conducted to verify the aforementioned analysis. Furthermore, optimization methods for efficiency improvement is included in this study.

**Author Contributions:** H.T., X.Y., and T.W. conceptualized the main idea of this research project; T.W. designed and conducted the experiments with the help of M.A. and X.L.; T.W., X.L., and N.J. checked and analyzed the results. T.W. wrote the whole paper; M.A. reviewed and edited the paper.

**Funding:** This work was funded by United Foundation of NSFC-Henan (U1604136).

**Conflicts of Interest:** The authors declare no conflict of interest.

## References

1. Asheer, S.; Al-Marawani, A.; Khattab, T.; Massoud, A. Inductive power transfer with wireless communication system for electric vehicles. In Proceedings of the 2013 7th IEEE GCC Conference and Exhibition, Doha, Qatar, 17–20 November 2013; pp. 517–522.
2. Musavi, F.; Eberle, W. Overview of wireless power transfer technologies for electric vehicle battery charging. *IET Power Electron.* **2014**, *7*, 60–66. [[CrossRef](#)]
3. Song, K.; Zhu, C.; Kim Ean, K.; Imura, T.; Hori, Y. Wireless power transfer for running EV powering using multi-parallel segmented rails. In Proceedings of the 2015 IEEE PELS Workshop on Emerging Technologies: Wireless Power, Daejeon, Korea, 5–6 June 2015.
4. Yin, N.; Xu, G.; Yang, Q.; Zhao, J.; Yang, X.; Jin, J.; Fu, W.; Sun, M. Analysis of wireless energy transmission for implantable device based on coupled magnetic resonance. *IEEE Trans. Magn.* **2012**, *48*, 723–726. [[CrossRef](#)]
5. Ma, A.; Poon, A.S.Y. Midfield wireless power transfer for bioelectronics. *IEEE Circuits Syst. Mag.* **2015**, *15*, 54–60. [[CrossRef](#)]
6. Huang, C.Y.; Boys, J.T.; Covic, G.A. LCL pickup circulating current controller for inductive power transfer systems. *IEEE Trans. Power Electron.* **2013**, *28*, 2081–2093. [[CrossRef](#)]
7. Qu, X.; Han, H.; Wong, S.C.; Chi, K.T.; Chen, W. Hybrid IPT topologies with constant current or constant voltage output for battery charging applications. *IEEE Trans. Power Electron.* **2015**, *30*, 6329–6337. [[CrossRef](#)]
8. Zhang, W.; Wong, S.C.; Chi, K.T.; Chen, Q. Analysis and comparison of secondary series- and parallel-compensated inductive power transfer systems operating for optimal efficiency and load-independent voltage-transfer ratio. *IEEE Trans. Power Electron.* **2014**, *29*, 2979–2990. [[CrossRef](#)]
9. Ge, S.; Liu, C.; Li, H.; Guo, Y.; Cai, G.W. Double-LCL resonant compensation network for electric vehicles wireless power transfer: Experimental study and analysis. *IET Power Electron.* **2016**, *9*, 2262–2270.
10. Sohn, Y.H.; Choi, B.H.; Lee, E.S.; Lim, G.C.; Cho, G.H.; Rim, C.T. General unified analyses of two-capacitor inductive power transfer systems: Equivalence of current-source SS and SP compensations. *IEEE Trans. Power Electron.* **2015**, *30*, 6030–6045. [[CrossRef](#)]
11. Tan, L.; Pan, S.; Xu, C.; Yan, C.; Liu, H.; Huang, X. Study of constant current-constant voltage output wireless charging system based on compound topologies. *J. Power Electron.* **2017**, *17*, 1109–1116.

12. Li, S.; Li, W.; Deng, J.; Nguyen, T.D.; Mi, C.C. A double-sided LCC compensation network and its tuning method for wireless power transfer. *IEEE Trans. Veh. Technol.* **2015**, *64*, 2261–2273. [[CrossRef](#)]
13. Xiao, C.; Cheng, D.; Wei, K. An LCC-C compensated wireless charging system for implantable cardiac pacemakers: Theory, experiment, and safety evaluation. *IEEE Trans. Power Electron.* **2018**, *33*, 4894–4905. [[CrossRef](#)]
14. Dai, X.; Li, W.; Li, Y.; Su, Y.; Tang, C.; Wang, Z.; Sun, Y. Improved LCL resonant network for inductive power transfer system. In Proceedings of the 2015 IEEE PELS Workshop on Emerging Technologies: Wireless Power (WoW), Daejeon, Korea, 5–6 June 2015.
15. Peng, F. Z-source inverter. *IEEE Trans. Ind. Appl.* **2003**, *39*, 504–510. [[CrossRef](#)]
16. Zeng, H.; Peng, F.Z. SiC based Z-source resonant converter with constant frequency and load regulation for EV wireless charger. *IEEE Trans. Power Electron.* **2017**, *32*, 8813–8822. [[CrossRef](#)]
17. Siwakoti, Y.P.; Town, G. Improved modulation Technique for voltage fed quasi-Z-source DC/DC converter. In Proceedings of the 2014 IEEE Applied Power Electronics Conference and Exposition (APEC), Fort Worth, TX, USA, 16–20 March 2014; pp. 1973–1978.
18. Wang, T.; Liu, X.; Tang, H.; Ali, M. Modification of the wireless power transfer system with Z-source inverter. *IET Electron. Lett.* **2017**, *53*, 106–108. [[CrossRef](#)]
19. Shen, M.; Peng, F. Operation modes and characteristics of the Z-source inverter with small inductance or low power factor. *IEEE Trans. Ind. Electron.* **2008**, *55*, 89–96. [[CrossRef](#)]
20. Sha, D.; You, F.; Wang, X. A high-efficiency current-fed semi-dual-active bridge DC-DC converter for low input voltage applications. *IEEE Trans. Ind. Electron.* **2016**, *63*, 2155–2164. [[CrossRef](#)]
21. Sha, D.; Wang, X.; Chen, D. High efficiency current-fed dual active bridge DC-DC converter with ZVS achievement throughout full range of load using optimized switching patterns. *IEEE Trans. Power Electron.* **2018**, *33*, 1347–1357. [[CrossRef](#)]
22. Fu, M.; Zhang, T.; Ma, C.; Zhang, X. Efficiency and optimal loads analysis for multiple-receiver wireless power transfer systems. *IEEE Trans. Microw. Theory Tech.* **2015**, *63*, 801–812. [[CrossRef](#)]
23. Liu, X.; Wang, T.; Yang, X.; Jin, N.; Tang, H. Analysis and design of a wireless power transfer system with dual active bridges. *Energies* **2017**, *10*, 1588. [[CrossRef](#)]
24. Sanborn, G.; Phipps, A. Standards and methods of power control for variable power bidirectional wireless power transfer. In Proceedings of the 2017 IEEE Wireless Power Transfer Conference (WPTC), Taipei, Taiwan, 10–12 May 2017.
25. Sha, D.; Wang, X.; Xu, Y. Unequal PWM control for a current-fed DC-DC converter for battery application. In Proceedings of the 2017 IEEE Applied Power Electronics Conference and Exposition (APEC), Tampa, FL, USA, 26–30 March 2017; pp. 3373–3377.
26. Kazimierczuk, M.K. Boost PWM DC-DC converter. In *Pulse-Width Modulated DC-DC Power Converters*, 2nd ed.; John Wiley & Sons, Wright State University: Dayton, OH, USA, 2017; Chapter 3, pp. 85–137.
27. Mai, R.; Liu, Y.; Li, Y.; Yue, P.; Cao, G.; He, Z. An active rectifier based maximum efficiency tracking method using an additional measurement coil for wireless power transfer. *IEEE Trans. Power Electron.* **2018**, *33*, 716–728. [[CrossRef](#)]
28. Liu, X.; Wang, T.; Yang, X.; Tang, H. Analysis of efficiency improvement in wireless power transfer system. *IET Power Electron.* **2018**, *11*, 302–309. [[CrossRef](#)]
29. Yang, E.X.; Lee, F.C.; Jovanovic, M.M. Small-signal modeling of series and parallel resonant converters. In Proceedings of the 1992 Applied Power Electronics Conference and Exposition (APEC), Boston, MA, USA, 23–27 February 1992; pp. 785–792.
30. Zhang, Y.; Chen, K.; He, F.; Zhao, Z.; Lu, T.; Yuan, L. Closed-form oriented modeling and analysis of wireless power transfer system with constant-voltage source and load. *IEEE Trans. Power Electron.* **2016**, *31*, 3472–3481. [[CrossRef](#)]

